2021

Cascaded multi-core vapor chambers for intra-package spreading of high power, heterogeneous heat loads,

S. Bandyopadhyay

A. M. Marconnet

Justin Weibel
jaweibel@purdue.edu

Bandyopadhyay, S.; Marconnet, A. M.; and Weibel, Justin, "Cascaded multi-core vapor chambers for intra-package spreading of high power, heterogeneous heat loads," (2021). *CTRC Research Publications.* Paper 383.
http://dx.doi.org/https://doi.org/10.1109/TCPMT.2021.3069953

Cascaded Multi-Core Vapor Chambers for Intra-Package Spreading of High Power, Heterogeneous Heat Loads

Soumya Bandyopadhyay, Amy M. Marconnet, Justin A. Weibel

***Abstract*—A cascaded multi-core vapor chamber (CMVC) is designed for dissipating heat from high-flux hotspots simultaneously with a high-total-power background. Current thermal management strategies rely on spreading high local heat fluxes by conduction in the lid of electronics packages. Embedding vapor chambers within the lid is an attractive option to directly address intra-package hotspots. We investigate the design of intra-lid vapor chambers, for a generic device having a total heat load of 476 W having a background heat flux of 0.75 W/mm^2, with hotspots of 8 W/mm^2 over a 1 mm^2 area. A conventional vapor chamber design, having a single vapor core, will require a thick evaporator wick to avoid the capillary limit for large total power. The necessity for a thick wick then imposes a large thermal conduction resistance when the vapor chamber is exposed to high heat flux hotspots. The proposed CMVC architecture aims to address this limitation. The cascaded architecture comprises a bottom-tier vapor chamber having an array of multiple small vapor cores for spreading heat from the small hotspots. These small vapor cores have short paths of liquid return to the evaporator, such that they can handle their footprint heat load while using thin wicks, resulting in a low hotspot thermal resistance. Furthermore, local dampening of the hotspots by the bottom tier then reduces the thermal conduction resistance across the necessarily thick wick in the top tier. Hence, the cascaded architecture has the potential to significantly reduce the overall thermal resistance, relative to a single tier. To substantiate this design rationale, experiments are performed to illustrate that the resistance of a commercial vapor chamber can be significantly reduced by interfacing the heat source with an intermediate heat spreader. Reduced-order models are then used to understand the effect of the wick properties (porosity and particle size) and geometric parameters on the thermal performance of the CMVC for the representative power map. The optimal CMVC design offers a thermal resistance (0.66 K/W) that is significantly lower compared to a conventional single-core vapor chamber (1.76 K/W) owing to a reduction in the conduction resistances across the internal wicks. That parametric optimization results demonstrate that the thermal resistance of the CMVC is more sensitive to the wick porosity compared to the particle diameter. Furthermore, there exists a wide range of wick properties and vapor core sizes for which near-optimum thermal performance can be attained, which is particularly attractive from the standpoint of flexibility in design and manufacturing.**

***Index Terms*—**Heterogeneous integration; electronics packaging; vapor chamber; capillary limit; cascaded multi-core vapor chamber (CMVC)

Manuscript received ## ##, 2021; revised ## #, 2021; accepted September 1, 2020. Date of publication ###, 2020; date of current version ####. This work was supported by the Semiconductor Research Corporation. Recommended for publication by Associate Editor #### upon evaluation of reviewers' comments. (Corresponding author: Justin A. Weibel.)

Soumya Bandyopadhyay, Amy M. Marconnet, and Justin A. Weibel are with the Cooling Technologies Research Center and the School of Mechanical Engineering, Purdue University, West Lafayette, IN 47907 USA (e-mail: bandyop0@purdue.edu; jaweibel@purdue.edu; marconnet@purdue.edu).

Color versions of one or more of the figures in this article are available online at https://ieeexplore.ieee.org. Digital Object Identifier #######

NOMENCLATURE

A	cross-sectional area
D	particle diameter
d	equivalent diameter
e	porosity
h	heat transfer coefficient
$h_{l,v}$	latent heat of vaporization
K	wick permeability
k	thermal conductivity
M	figure of merit for a vapor chamber
P	pressure
Q	heat input
R	thermal resistance
r	pore radius
T	temperature
$T_{f,in}$	recirculating bath fluid temperature
T_{inf}	inlet air temperature to the heat sink
t	thickness
x	length

Greek Symbols

ρ	density
σ	surface tension
μ	dynamic viscosity

Subscripts

b	bottom tier of CMVC
l	liquid
cap	capillary limit
chs	core over hotspot
cp	cold plate
$cond$	condenser
$conv$	convection

I. INTRODUCTION

The next revolution in thermal packaging will be the heterogeneous integration of multiple different components and devices into a single package for enhanced functionality. This new packaging paradigm will exacerbate the non-uniformity of package-internal heat generation, requiring novel thermal solutions capable of spreading heat from the internal dies that have a high total peak power simultaneous with extreme local heat fluxes. The device performance is significantly affected by internal package thermal resistances and heat spreading from local hotspots. In typical heterogeneous 2.5D packages, the package lid must effectively spread heat from the internal die.

Vapor chamber devices passively spread heat from a concentrated input area (the evaporator) to a comparatively larger area (the condenser), where the heat is then dissipated to a heat sink or cold plate. Vapor chambers comprise a sealed cavity lined on the inside by capillary porous wick structures that passively pump an internal working fluid. Liquid continuously provided to the evaporator wick evaporates as it receives heat from the source. The vapor thus generated at the

evaporator flows through the inner core and condenses on the condenser wick. Ultimately heat is dissipated from the condenser side to the heat sink. This passive two-phase cycle transports heat at a smaller temperature difference relative to conduction and spreading in solid heat spreaders. Consequently, vapor chambers have been employed in numerous thermal management applications spanning a wide range of form factors and power levels. Hence, the development of vapor chamber concepts appropriate for integration into high-power heterogeneous packages, specifically to address the outstanding challenge of hotspots, may enable reliable operation even with the continued rise in the thermal design power of next-generation electronics [1].

There have been extensive recent investigations focusing on the design of evaporator wick structures inside of a vapor chamber to address the removal of high heat fluxes over differing heat input areas, as reviewed by Weibel and Garimella [2]. Monoporous wicks, sintered metal powders, and screens generally provide higher capillary pressure head and effective thermal conductivities relative to other conventional wick structures [3]. Weibel et al. [4] explored the dependence of wick thickness and particle size on the thermal performance of monoporous sintered powder wicks under capillary-fed evaporation and boiling, with the experimental demonstration of the dissipation of heat fluxes of > 500 W/cm^2. Li et al. [5,6] identified and investigated the critical parameters governing the two-phase heat transfer from sintered copper screen meshes. Chen et al. [7] experimentally studied the influence of the charging quantity of the working fluid on the relative thermal performance of aluminum vapor chambers with sintered powder and radially groove wicks.

Several studies have focused on the development of wick structures for dissipation of a high total power over relatively large evaporator areas at uniform heat fluxes. Hwang *et al.* [8] placed multiple wick columns connecting the condenser to the evaporator in a vapor chamber to spread ~380 W/cm^2 from a heat input area of 1 cm^2, with a surface superheat ~ 20 K. Hybrid evaporator wicks designed and experimentally characterized by Ju *et al.* [9] dissipated heat fluxes exceeding 375 W/cm^2 over a 4 cm^2 evaporator area, achieved by integrating a network of high-permeability liquid supply structures with sintered copper monolayer wicks. Weibel *et al.* [10] examined grid-patterned sintered wick structures for removal of heat fluxes exceeding 500 W/cm^2 over a 0.25 cm^2 evaporator area. This study demonstrated the reduction in effective thermal resistance due to boiling incipience, and operating in a capillary-fed regime, compared to evaporation. Semenic *et al.* [11] experimentally demonstrated the dissipation of 520 W/cm^2 originating from a ~0.3 cm^2 evaporator using thin biporous sintered wicks, at a surface superheat of 50 K. Recently, Sudhakar *et al.* [12,13] demonstrated a two-layer evaporator wick designed for dissipating high heat fluxes of 512 W/cm^2 from a comparatively larger heat input area of 1 cm^2 while maintaining a thermal resistance of 0.08 K/W.

Alternatively, several studies have explored wicks that are effective in dissipating extremely high heat fluxes from smaller hotspot areas. Cai and Bhunia [14] showed that heat flux densities of 770 W/cm^2 were dissipated over 0.04 cm^2 s a surface superheat of ~35 K using striped carbon nanotube (CNT) bi-porous structures. The dissipation of even higher heat fluxes of 938 W/cm^2 over 0.04 cm^2 was subsequently demonstrated using bi-porous CNT wicks [15]. However, as the heated area was increased up to 1 cm^2, the dry out heat flux reduced significantly to 195 W/cm^2. Palko *et al.* [16] showed that copper inverse opal wicks were capable of dissipating extremely high heat fluxes > 1200 W/cm^2, albeit over a very small area of ~0.006 cm^2, during capillary-fed boiling. The study revealed that fine (5 µm) wick features enabled extremely low superheats < 10 K at these extreme heat fluxes, but limited the areas over which they could operate due to their low permeability.

Despite practical relevance, a noteworthy omission from past literature is the design and development of evaporator wicks and vapor chambers designs with the express purpose of managing power maps that include both high total powers (over large areas) and small hotpots, appearing simultaneously. Our recent work introduced the concept of an intra-lid cascaded multi-core vapor chamber (CMVC) [17] to spread large total heat loads from the entire die area, while also minimizing the temperature rise associated with high heat flux hotspots. The current work performs a detailed design optimization of the CMVC to evaluate the performance sensitivity to a range of parameters and thereby offers new insight into the flexibility of design in the context of manufacturing and subsequent intra-lid integration in an electronic package. Separately, new experiments are performed to demonstrate that the thermal resistance of a given commercial vapor chamber can be reduced by interfacing it with another vapor chamber placed directly over the heat source. This demonstration confirms one of the principal elements motivating the design of the CMVC, that a performance improvement can be achieved in the top-tier via a reduction in the conduction resistances across the internal wick. The reduced-order thermal model is then used to optimize the design of the CMVC and compare its thermal resistance to a conventional vapor chamber and a solid copper benchmark. Finally, we examine the relative sensitivity of the various design parameters towards gaining an understanding of the potential range of parameters that can yield near-optimal thermal performance.

II. Cascaded Multi-Core Vapor Chamber

The intra-lid CMVC concept [17], as depicted in Fig. 1, decouples the spreading of the total background die power from that of individual hotspots using two cascaded tiers: a top-tier single vapor core for bulk heat spreading and a bottom-tier, multi-core vapor chamber for damping of local hotspots that may appear anywhere over its footprint. It is important to note that while both the tiers are thermally coupled, they are sealed off from each other and hydraulically independent. The top tier effectively serves as a conventional vapor chamber that spreads the total heat load to the significantly large base area of the mounted heat sink. The bottom tier (see Fig. 1 inset), which covers the heat source area, contains an array of smaller vapor cores that are designed to spread the high heat fluxes originating from the individual hotspots to a slightly larger area. Coverage of the heat source with multiple vapor cores ensures that a hotspot formed in any location will be spread out by the core above. The small size of each core appreciably reduces the

pressure drop of the recirculating working liquid by minimizing the flow length from its condenser to the evaporator. Consequently, each core in the bottom tier can sustain operation at the same capillary-limited heat load as the top tier, but with significantly thinner wicks. The bottom tier thus attenuates the high hotspot fluxes while imposing a small conduction resistance across the thin wicks before heat is transferred into the top tier, which requires thicker wicks to manage the total heat load within the capillary limit. This paper explores, using a reduced-order modeling framework, design optimization of the CMVC to minimize its thermal resistance when subjected to a nonuniform power map having a high total background heat load with high heat flux hotspot. The optimized CMVC thermal resistance is compared to that of a solid copper heat spreader and a conventional vapor chamber.

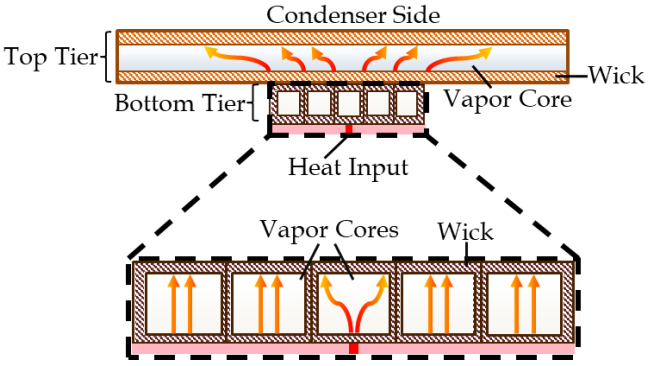

Fig. 1. Schematic cross-sectional drawing (not to scale) of the cascaded multi-core vapor chamber with inset magnified view of the bottom tier having an array of small vapor cores. Note the background heat input is over the entire width of the bottom tier (light pink bar) and dark red portions indicate localized smaller hotspots.

III. Modeling and Design Approach

A reduced-order model evaluates the thermal resistance of different candidate intra-lid heat spreaders: a solid copper benchmark, a conventional vapor chamber, and the CMVC, as introduced in Fig. 2 (adapted from [17]).

For a fair comparison, the available design envelope and power map are kept fixed across all heat spreaders, while the remaining free design parameters are optimized independently for each spreader type. The available design envelope constrains the spreaders to have a maximum through-plane thickness (t) of 2 mm within a square cross-section having an edge length (x_{sp}) of 55 mm. They are all subjected to the same representative nonuniform power map from a square die having an edge length (x_{die}) of 25 mm. A hotspot heat load (Q_{hs}) of 8 W over 1 mm^2 (denoted by dark red) is located in the center of the die, and the remaining area has a uniform background flux of 0.75 W/mm^2 (denoted by light pink). For the CMVC, the hotspot is centrally located underneath one of the vapor cores of the bottom tier. Because the performance of heat spreaders is influenced by the value of the thermal resistance to heat rejection, for purposes of this analysis, this value is calculated assuming the performance of a typical air-cooled heatsink [18] attached to the heat spreader using a high-performance thermal interface material. The external thermal resistance (R_{ext} = 0.15 K/W) from the spreader-TIM interface to the reference temperature (T_{inf} = 300 K) is calculated as:

$$R_{ext} = R_{TIM} + R_{conv}. \quad (1)$$

This thermal resistance results in an effective heat transfer coefficient (h) of 2250 W/m^{2}K at the spreader-TIM interface. The temperature at the spreader-TIM interface can be computed from the total die heat load (Q_{die}), as:

$$T_{cond,t} = T_{inf} + Q_{die} R_{ext}. \quad (2)$$

Details of the reduced-order modeling approach, design of the wick thickness, and the parametric optimization approach are described in the subsections that follow.

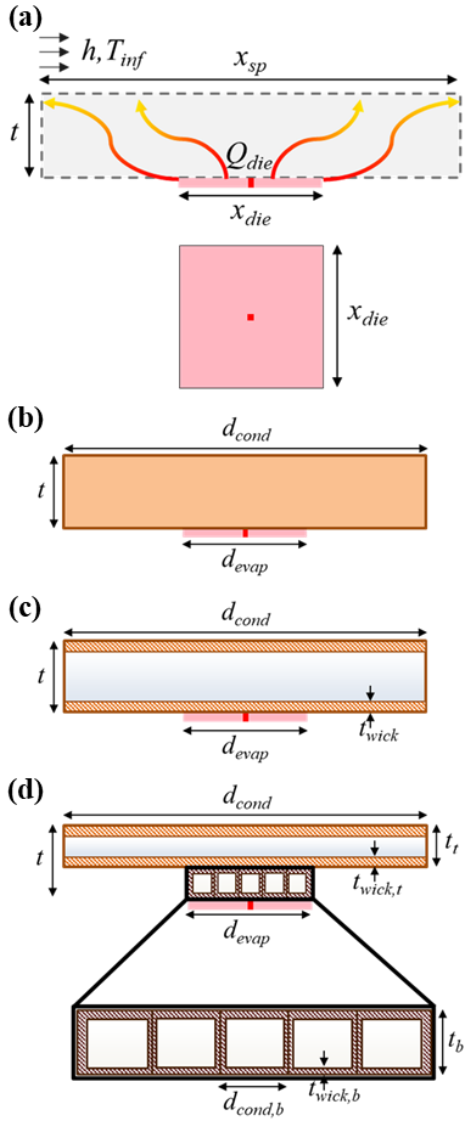

Fig. 2. (a) Cross-sectional and bottom view schematics of heat transfer problem. The die consists of a region with a low background heat flux (light) with a small hot spot at the center (dark). The dashed gray box illustrates the location for one of three heat spreading solutions ((b) solid copper, (c) conventional single-core vapor chamber, and (d) cascaded multi-core vapor chamber (CMVC), shown as cross-sections) that spread heat from the die to the heat sink (modeled with a heat transfer coefficient and free stream temperature). Wicks are illustrated with hashed regions in the cross-sectional schematics in panels b-d. All parameters varied during the parametric design optimization are shown, including the fixed equivalent design envelope parameters (d_{evap}, d_{cond}, and t). In panel (d), the inset shows a magnified view of the bottom tier with multiple cores.

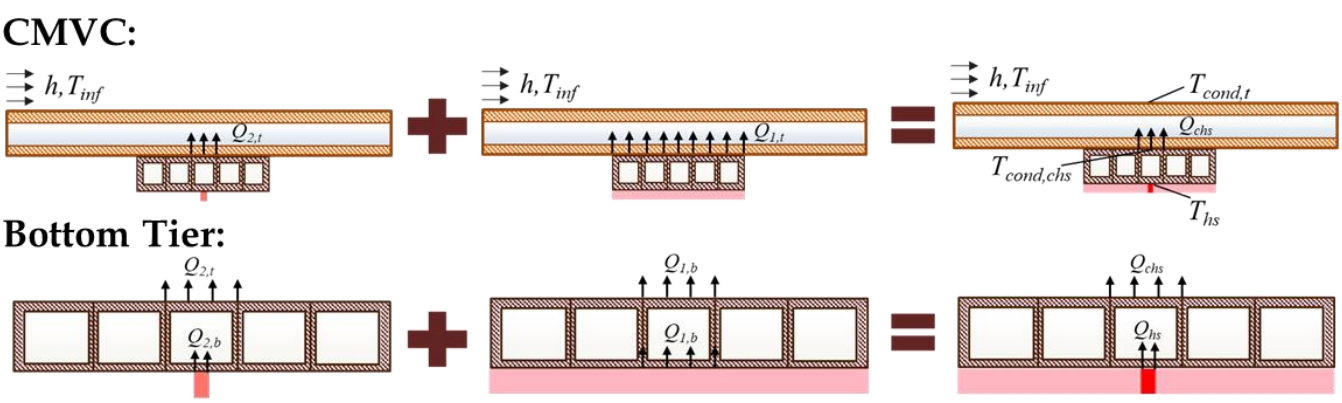

Fig. 3. Schematic cross-section of the cascaded multi-core vapor chamber (CMVC) depicting the heat flow paths and the heat loads through the bottom tier cores (magnified view) into the top tier, illustrating the principle of superposition.

A. Reduced-order model

The heat spreaders are modeled as cylindrical disks with effective radii that yield the same equivalent heat input and condenser areas as the rectangular geometry. The solid copper heat spreader resistance due to conduction is calculated as a function of the geometry and boundary conditions using the correlations provided by Song *et al.* [19]. The vapor chamber thermal resistance for a given uniform heat input is estimated based on one-dimensional conduction across the wicks and the temperature drop across the vapor core due to the saturation pressure difference (for details, refer to Ref. [20]); the resistance due to phase change at the interface is neglected. For evaluation of the vapor pressure drop, the thermophysical properties are taken at the temperature corresponding to the spreader-TIM interface.

For the given non-uniform power map, the maximum die temperature and the corresponding thermal resistance will occur at the hotspot location. To calculate the maximum thermal resistance for the solid copper and the conventional vapor chamber (R_{sp}), the total heat load of the power map is decomposed into a 468.75 W heat input (Q_1) at a uniform flux of 0.75 W/mm^2 over the entire die area and a 7.25 W heat input (Q_2) over the 1 mm^2 hotspot. The total temperature difference between the hotspot and the spreader-TIM interface (ΔT_{hs}) is computed from the thermal resistances associated with the decomposed heat inputs, respectively R_1 and R_2 as estimated from the reduced-order models, using the principle of linear superposition:

$$\Delta T_{hs} = Q_1 R_1 + Q_2 R_2. \tag{3}$$

This net hotspot temperature difference (ΔT_{hs}) and the heat load at the hotspot (Q_{hs}) are employed to compute the maximum spreader resistance as:

$$R_{sp} = \frac{\Delta T_{hs}}{Q_{hs}}. \tag{4}$$

For the bottom-tier core that is located directly over the hotspot of the die, it is considered that the total heat input to this core is spread uniformly over the condenser wick, and there is a uniform heat flux into the top tier evaporator wick dictated by the cross-sectional area ($A_{cond,b}$) of the bottom-tier core. Fig. 3 shows the cross-section of the CMVC with the heat flow paths and the heat loads in each tier. The maximum thermal resistance for the bottom tier ($R_{sp,b}$) is computed by decomposing the total heat load (see Fig. 3) handled by this particular vapor core into a heat input ($Q_{1,b}$) distributed uniformly over the entire vapor core at 0.75 W/mm^2 and the concentrated heat input ($Q_{2,b}$) of 7.25 W over the 1 mm^2 hotspot. The respective thermal resistances, $R_{1,b}$ and $R_{2,b}$, as computed from the reduced-order models, are employed to estimate the total difference between the temperatures of the hotspot (T_{hs}) and the condenser side of the bottom-tier core ($T_{cond,chs}$), as:

$$T_{hs} - T_{cond,chs} = Q_{1,b} R_{1,b} + Q_{2,b} R_{2,b}. \tag{5}$$

This net temperature difference and the total heat input at the hotspot (Q_{hs}) are employed to compute the resistance of the bottom tier as:

$$R_{sp,b} = \frac{T_{hs} - T_{cond,chs}}{Q_{hs}}. \tag{6}$$

This net temperature difference and the total heat input at the hotspot (Q_{hs}) are employed to compute the resistance of the bottom tier as:

$$T_{cond,chs} - T_{cond,t} = Q_{1,t} R_{1,t} + Q_{2,t} R_{2,t}. \tag{7}$$

This temperature difference and the heat load for the hotspot (Q_{hs}) are employed to compute the thermal resistance of the top tier as:

$$R_{sp,t} = \frac{T_{cond,chs} - T_{cond,t}}{Q_{hs}}. \tag{8}$$

To evaluate the maximum spreader thermal resistance (R_{sp}) for the CMVC using Eq. (4), the net temperature difference between the hotspot and the CMVC condenser (ΔT_{hs}) is calculated as:

$$\Delta T_{hs} = T_{hs} - T_{cond,t} = Q_{hs}\left(R_{sp,b} + R_{sp,t}\right). \tag{9}$$

B. Design of wick thicknesses

The vapor chamber wicks are designed to have the minimum possible thickness without reaching the capillary limit at the required total heat load; this corresponds to the possible conduction thermal resistance. This minimum wick thickness for a given vapor chamber (or individual core within the bottom-tier array) is dictated by the balance between the total liquid pressure drop (ΔP_l) and the available capillary pressure (ΔP_{cap}). The liquid pressure drop (ΔP) for a given uniform heat input (Q) over the entire evaporator area is estimated by considering a one-dimensional radial flow through the evaporator and the condenser wicks according to Darcy's law for porous materials:

$$\Delta P = \frac{\mu_l Q}{2\pi h_{l,v} \rho_l K t_{cap}} \left(\ln\left(\frac{d_{cond}}{d_{evap}} \right) + 1 \right). \tag{10}$$

For the representative nonuniform power map, the liquid pressure drops (ΔP_1) and (ΔP_2) are respectively computed using Eq. (10) from the decomposed uniform heat inputs Q_1 and Q_2 defined in Section 3.1. The total pressure drop of the liquid, employing the principle of linear superposition, is estimated as:

$$\Delta P_l = \Delta P_1 + \Delta P_2. \tag{11}$$

The driving capillary pressure head is computed from an effective pore radius of the wick and assuming perfect wettability as:

$$\Delta P_{cap} = \frac{2\sigma_l}{r_{eff}}. \tag{12}$$

Owing to their high capillary pressure and effective thermal conductivity, this study considers sintered copper particle wicks. The effective pore radius (r_{eff}) and the permeability (K) of the wick can be estimated [3] as a function of the wick porosity (e) and the particle diameter (D), as:

$$r_{eff} = 0.21D, \text{ and} \tag{13}$$

$$K = \frac{D^2 e^3}{150(1-e)^2}. \tag{14}$$

The capillary-limit-governed thickness of the wick (t_{cap}) is obtained by equating ΔP_l to ΔP_{cap}, and depends on the ratio of the effective pore radius and the permeability of the wick:

$$\Delta P_l = \Delta P_{cap} \Rightarrow t_{cap} = \frac{Q_1 r_{eff}}{4\pi M_l K} \left\{ \ln\left(\frac{d_{cond}}{d_{evap}} \right) + 1 \right\} + \frac{Q_2 r_{eff}}{4\pi M_l K} \left\{ \ln\left(\frac{d_{cond}}{d_{hs}} \right) + 1 \right\}. \tag{15}$$

where, $M_l = (\rho_l \sigma_l h_{l,v})/\mu_l$, is the liquid figure of merit. An additional constraint is imposed to ensure that the sintered copper wicks have a minimum thickness of at least three particle diameters. Hence, the designed wick thickness (t_{wick}) becomes set based on the maximum of either the capillary-limited thickness or this three-particle constraint:

$$t_{wick} = \max(t_{cap}, 3D). \tag{16}$$

For the CMVC, this same design approach has been adapted to the individual tiers by calculating the total pressure drop ($\Delta P_{l,b}$) in the bottom tier using the decomposed heat inputs $Q_{1,b}$ and $Q_{2,b}$ defined in Section 3.1, and equating to the capillary pressure ($\Delta P_{cap,b}$) to design the wick thickness ($t_{wick,b}$). Separately, the balance between the capillary pressure ($\Delta P_{cap,t}$) and the total liquid pressure drop ($\Delta P_{l,t}$) in the top tier, computed with $Q_{1,t}$ and $Q_{2,t}$, is used to design the wick thickness in the top tier ($t_{wick,t}$).

C. Parametric design optimization

For each heat spreader type, a parametric optimization is performed to minimize the thermal resistance (R_{sp}) for the same equivalent cylindrical design envelope dimensions (d_{cond}, t) and power map. Fig. 2 shows the key parameters that are varied for the solid copper, the conventional vapor chamber, and the CMVC.

The thermal resistance of the solid copper heat spreader is governed by only its thickness (t) and cross-sectional area. The minimum resistance is obtained for the trivial case where copper occupies the entire design envelope.

For the vapor chambers, water is considered as the working fluid. Furthermore, the thickness of copper walls is neglected for the vapor chambers, such that the vapor core and wick occupy the entire design envelope when comparing their performance with the solid copper. As described in Section 3.1, the total thermal resistance is dictated by one-dimensional heat conduction across the wicks and heat spreading in the vapor core. Because the wick thickness is minimized (as described in Section 3.2), this determines the vapor core thickness and the associated thermal resistance. The thermal resistance resulting from heat conduction in the wicks (R_{wick}) is determined by the effective thermal conductivity of the sintered copper powder, the designed wick thickness, and the area corresponding to a given heat load (A_{hl}); because the designed wick thickness is constrained per Eq. (16), these conduction thermal resistances are inherently a function of the porosity, particle diameter, and permeability, as:

$$R_{wick} = \frac{t_{wick}}{k_{wick} A_{hl}} = f(e, D, K). \tag{17}$$

For the conventional vapor chamber, because there is only a single core, the designed wick thickness (t_{wick}) sets the vapor core thickness based on the available total design envelope thickness (t). The vapor core thermal resistance accounts for the in-plane heat spreading and the associated three-dimensional variation in temperature. For the design envelope thickness and power map considered in this study, it has been experimentally demonstrated [17] that the thermal resistance resulting from the difference in saturation pressure in the vapor core (R_{vap}) is always orders lower than the conduction resistance across the wicks and is therefore neglected. For the parametric design optimization, the porosity is varied between 0.42 and 0.6, and

the particle diameter is varied between 5 µm and 75 µm, corresponding to the approximate range of reasonable parameters for sintered copper wicks.

For the CMVC, the parametric investigation is extended to allow the thicknesses of the individual tiers (t_t, t_b) to vary within the available design thickness (t). Furthermore, the number and diameter of cores ($d_{cond,b}$) in the bottom tier array are free to vary and influence the heat flux levels at the evaporator of the top tier, which consequently affects the design of the wick thickness ($t_{wick,t}$, $t_{wick,b}$)and the vapor core thicknesses (t_t, t_b) of the individual tiers. The porosities (e_t, e_b) and particle diameters (D_t, D_b) of the wicks of the individual tiers are varied between the same bounds as the conventional vapor chamber. A custom MATLAB script executes the reduced-order model throughout the design space to identify the parameters which offer the lowest thermal resistance.

IV. Experimental Methods

Here, we illustrate the key design rationale behind the use of a cascade of stacked vapor chambers through an experiment. Specifically, we demonstrate that the thermal resistance of a vapor chamber (analogous to the top tier) can be significantly reduced by the introduction of a buffer vapor chamber placed below to first diffuse hotspots. This is achieved by characterizing the thermal resistance of a standalone vapor chamber, and the same vapor chamber but interfaced with a smaller footprint buffer vapor chamber placed below. Fig. 4(a) shows the cross-sections of the standalone and interfaced vapor chambers. The testing is performed using commercially available vapor chambers having dimensions 90 mm × 90 mm × 3 mm (345-1564-ND, Wakefield Vette) and 30 mm × 30 mm × 3 mm (Novark). Note these are both commercially available vapor chambers and have not been optimized for the cascaded multi-core vapor chamber architecture discussed above, and thus we term the combination an "interfaced vapor chamber" rather than CMVC.

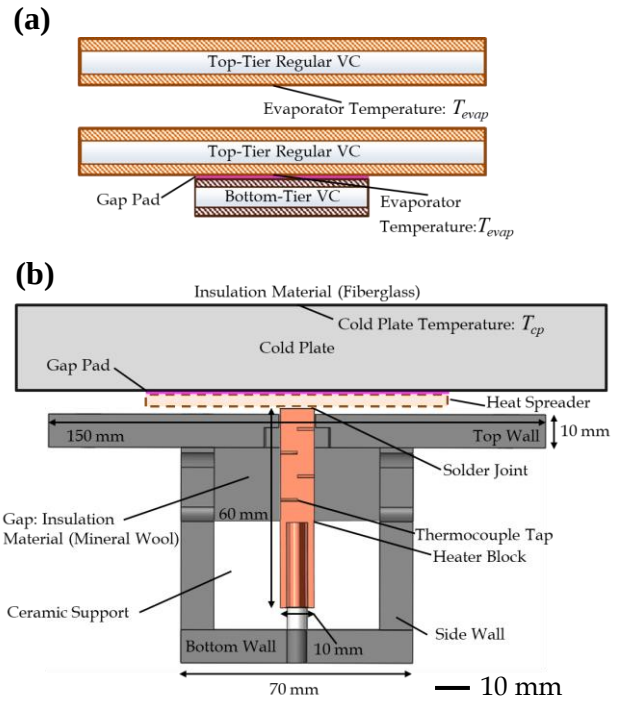

Fig. 4. (a) Schematic cross-sections of the two cases of the heat spreader: a standalone regular vapor chamber, and a regular vapor chamber interfaced with a buffer vapor chamber. Thermocouples measure the temperature of the evaporator of the regular vapor chamber and the cold plate. (b) Section view of the experimental facility for characterization of a heat spreader. A copper heater block insulated by a ceramic support and PEEK wall provides a uniform heat flux to the base of the heat spreader soldered atop. Thermocouples that measure the temperature gradient along the centerline of the copper block are used to determine the heat flux and temperature at the base of the heat spreader.

A. Experimental facility

The experimental facility shown in Fig. 4(b) was previously reported in [17] to evaluate the thermal resistance of heat spreaders at differing temperatures and heat loads and is briefly reviewed here. Vapor chambers are attached to the top 10 mm × 10 mm surface of an insulated oxygen-free copper block, heated by a cartridge heater. The copper block has a rake of thermocouples positioned along its centerline to measure the heat flux and extrapolate the surface temperature. The vapor chambers are attached to the top of the heater block using an in-house low-temperature soldering process [17]. The condenser surface of the top vapor chamber is interfaced with the bottom surface of a cold plate (416101U00000G, Aavid Thermalloy) via a thermal gap pad (Tflex™ HD700, Laird). For the experiments with two cascaded vapor chambers, the top vapor chamber is interfaced with the buffer vapor chamber using the same type of gap pad. Deionized water is pumped through the cold plate (insulated on top) with a refrigerating bath circulator (RW-0525G, Lab Companion).

B. Testing procedure

Experiments are run at an electrical power input corresponding to 23.5 W/cm^2. The liquid temperature ($T_{f,in}$) in the refrigerating bath circulator is incremented in steps from 50 °C to 80 °C, and steady-state data are recorded for each step when the block temperatures change of less than 0.01 °C/s. Data

acquired at a maximum frequency of 0.33 Hz are averaged over 30 min (~600 data points) and reported as steady-state values. Because the recirculating bath fluid temperature corresponds to the mean operating vapor temperature in the vapor chamber, this procedure would reveal any influence of the operating temperature on the performance.

C. Data reduction and uncertainty

All thermocouples used for temperature measurement are ice-point-referenced (TRCIll, Omega) and calibrated using a dry-block calibrator (Jupiter 4852 Advanced, Isotech). The temperature gradient measured from the linear fit to the four thermocouples inside the copper heater block is employed to estimate the actual heat flux and the resulting heat load (Q_{vc}) into the vapor chamber. Uncertainty in the measured heat flux is estimated to be less than 4% based on the calibrated uncertainties in the temperature (± 0.2 ℃) and the location of the measurements. All uncertainties are calculated as described in Ref. [21].

The temperature at the evaporator (T_{evap}) of the conventional vapor chamber is measured by laying a thermocouple (± 0.6 ℃) into a shallow groove fabricated on the bottom surface of the vapor chamber. The temperature at the top surface of the cold plate (T_{cp}) is estimated from an average of four thermocouple measurements distributed over the surface. The thermal resistance is then calculated based on the difference between the evaporator and cold plate temperatures, as:

$$R_{evap,cp} = \frac{T_{evap} - T_{cp}}{Q_{vc}}. \tag{18}$$

III. Results

First, the predictions from the experiments using commercial vapor chambers are presented and discussed. Next, the reduced-order model is used to explore the effect of the porosity and particle diameter on the designed wick thickness and the thermal resistance of the top tier and the bottom tier of the cascaded multi-core vapor chamber (CMVC). Finally, we discuss the relative optimized performance of the solid copper benchmark, the conventional single-core vapor chamber, and the CMVC, as predicted from the reduced-order model.

A. Experiment: Influence of buffer vapor chamber

Fig. 5 shows the measured thermal resistance as a function of the recirculating bath fluid temperature for the two test cases shown in Fig. 4(a). This measured thermal resistance for both the standalone vapor chamber (dashed blue line) and the interfaced vapor chamber (dashed green line) is observed to be independent of the operating temperature (within the uncertainty limits) for the range tested. This is attributed to the dominance of the temperature-independent conduction resistances across the wicks [17] relative to the vapor core thermal resistance. Notably, the vapor chamber thermal resistance of 0.52 K/W (corresponding to a temperature difference of 9.7 ℃ at the input heat load of 18.5 W) reduces significantly when the buffer vapor chamber is introduced to 0.22 K/W (a difference of 4.0 ℃ at 18.2 W). This indicates that the buffer vapor chamber effectively spreads out the heat load before it enters the vapor chamber above. This result supports the CMVC design rationale, as it confirms the effectiveness of the buffer vapor chamber in dampening the heat flux to improve the performance of the top vapor chamber, even from this 10 mm × 10 mm heat input area, and have promise for further improvements for smaller hotspots.

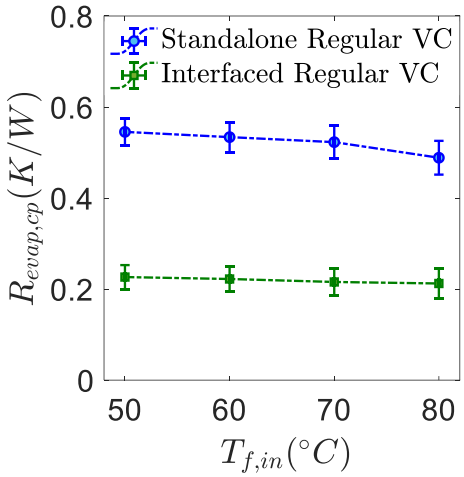

Fig. 5. Thermal resistance for the standalone vapor chamber (VC) compared to the performance of the same vapor chamber with the addition of a buffer vapor chamber ("interfaced regular VC"). For the interfaced regular VC, the addition of the buffer vapor chamber reduces the thermal resistance of the conventional vapor chamber and performance is relatively insensitive to $T_{f,in}$

B. Parametric effects on performance: conventional vapor chamber

The contour plots in Fig. 6 (a) and (b) depict the variation of the designed wick thickness (t_{wick}) and the maximum thermal resistance (R_{sp}) of the conventional single-core vapor chamber, respectively, as a function of the wick porosity (e) and the particle diameter (D) for the nonuniform power map. In general, the designed wick thickness reduces with the decrease in particle diameter and the increase in the wick porosity.

For a given particle diameter, there exists a transitional porosity (noted by the white dashed lines) above which the designed wick thickness is governed by the particle diameter constraint per Eq. (16) (below this line the wick thickness is governed by the capillary limit). This is attributed to a reduction in the capillary-limit-governed wick thickness (t_{cap}) because of the increase in the wick permeability. With an increase in the particle diameter, there is a reduction in the driving capillary pressure head (ΔP_{cap}) (see Eq. (12)); furthermore, the wick permeability increases (see Eq. (14)) with an increase in the particle diameter. Hence, with an increase in the particle diameter, the transition of the design from a capillary-limit-governed wick thickness ($t_{wick} = t_{cap}$) to a particle diameter-governed wick thickness ($t_{wick} = 3D$) occurs at a lower wick porosity.

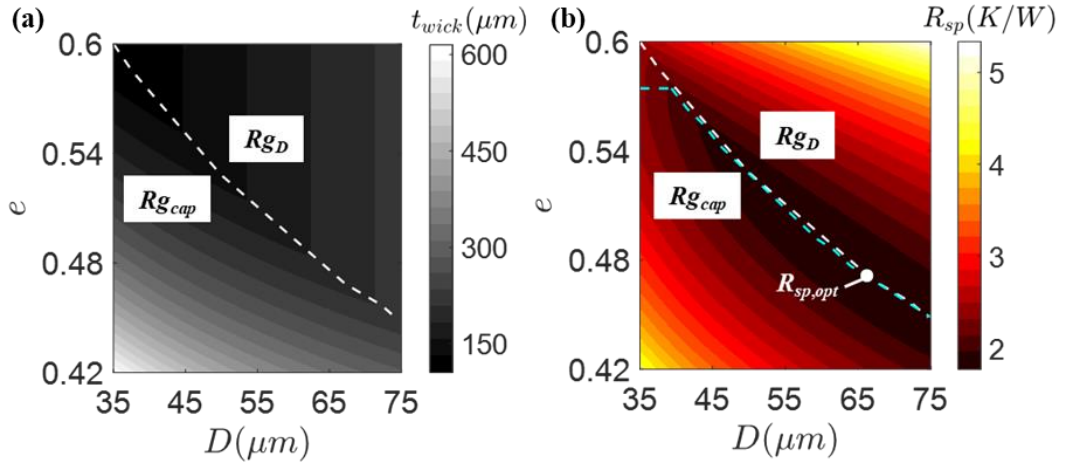

Fig. 6. (a) Designed wick thickness (t_{wick}) and (b) maximum thermal resistance (R_{sp}) for a conventional single-core vapor chamber as a function of wick porosity e and particle diameter D for a total thickness t = 2 mm. The regions (Rg) to the left and right of the white dashed line correspond to the capillary-limit-governed wick thickness (Rg_{cap}: $t_{wick} = t_{cap}$) and the particle diameter-governed wick thickness (Rg_D: $t_{wick} = 3D$), respectively. The blue dashed line in (b) denotes the porosity e for which the thermal resistance R_{sp} is minimum for any given particle diameter D. The point of optimal thermal resistance for a conventional vapor chamber is denoted by the white dot labeled $R_{sp,opt}$ in (b).

The thermal resistance (R_{sp}) of the conventional vapor chamber is dominated by the conduction resistance across the wicks (~10^4 times the vapor core thermal resistance). The minimum thermal resistance (dashed blue line in Fig. 6(b)) corresponding to a given particle diameter occurs at a constant value of porosity (e = 0.57) until D = 40 µm. In this region, the thermal resistance (R_{sp}) is determined by conduction across the capillary-limit-governed wick thickness. The particular value of optimum porosity in this region, which offers the minimum resistance, is governed by the tradeoff between an increasing capillary-limited wick thickness and increasing wick thermal conductivity with porosity. For a given particle diameter greater than 40 µm, the designed wick thickness reduces until it becomes governed by the three-particle diameter constraint, rather than the capillary limit. This reduction in the wick thickness dominates over the decrease in wick thermal conductivity, with an increase in wick porosity from 0.5 till the transitional porosity of 0.57. Consequently, the minimum thermal resistance, in this particle diameter-governed region, is determined by the wick thickness at the transitional porosity (i.e., the blue and white dashed lines overlap).

This parametric design optimization of the conventional vapor chamber yields an optimal porosity (e_{opt}) of 0.47 particle diameter (D_{opt}) of 66 µm, and wick thickness ($t_{wick,opt}$) of 199 µm having an optimized thermal resistance of 1.76 K/W. At the optimum, the thermal resistance is more sensitive to the porosity compared to the particle diameter (e.g., increases to 2.31 K/W versus 1.94 K/W with 10% increase in e and D, respectively). The thermal resistance isocontours shown in Fig. 6(b) reveal that there is a design window of wick porosities and the particle diameters for which the thermal resistance of the conventional vapor chamber will be near the optimized value (< 2 K/W).

C. Parametric effects on performance: CMVC

Figure 7 show the variation of the designed wick thicknesses ($t_{wick,t}$ and$t_{wick,b}$) and the thermal resistances ($R_{sp,t}$, $R_{sp,b}$) for the top and bottom tiers of the CMVC (t_t = 1.4 mm, t_b = 0.6 mm, $d_{cond,b}$ = 5.0 mm), for the nonuniform power map. The specific trends within these data follow the same behavior (and interpretation) as previously shown for the single-core vapor chamber in Fig. 6, but result in different optimal design parameters for the CMVC. The optimized thermal resistance ($R_{sp,t,opt}$ = 0.27 K/W; $R_{sp,b,opt}$ = 0.38 K/W) is obtained for a top tier ($e_{t,opt}$ = 0.47; $D_{t,opt}$ = 65 µm; $t_{wick,t,opt}$ = 195 µm) thickness ($t_{t,opt}$) of 1.4 mm and an optimal bottom tier ($e_{b,opt}$ = 0.47; $D_{b,opt}$ = 13 µm; $t_{wick,b,opt}$ = 39 µm) core diameter ($d_{cond,b,opt}$) of 5.0 mm.

These optimal wick parameters reveal the need for thinner wicks and lower particle diameters for the bottom tier, relative to the top tier, to avoid the capillary limit. This is attributed to the large total heat loads in the top tier compared to a single core of the bottom tier. As in the case of the conventional vapor chamber, at the optimal wick parameters, the thermal resistance of the individual tiers is more sensitive to the porosity compared to the particle diameter, and the thermal resistance isocontours shown in Fig. 7(b,d) reveal the design windows of porosities and particle diameters for which the thermal resistance of the tiers will be near their optimized values.

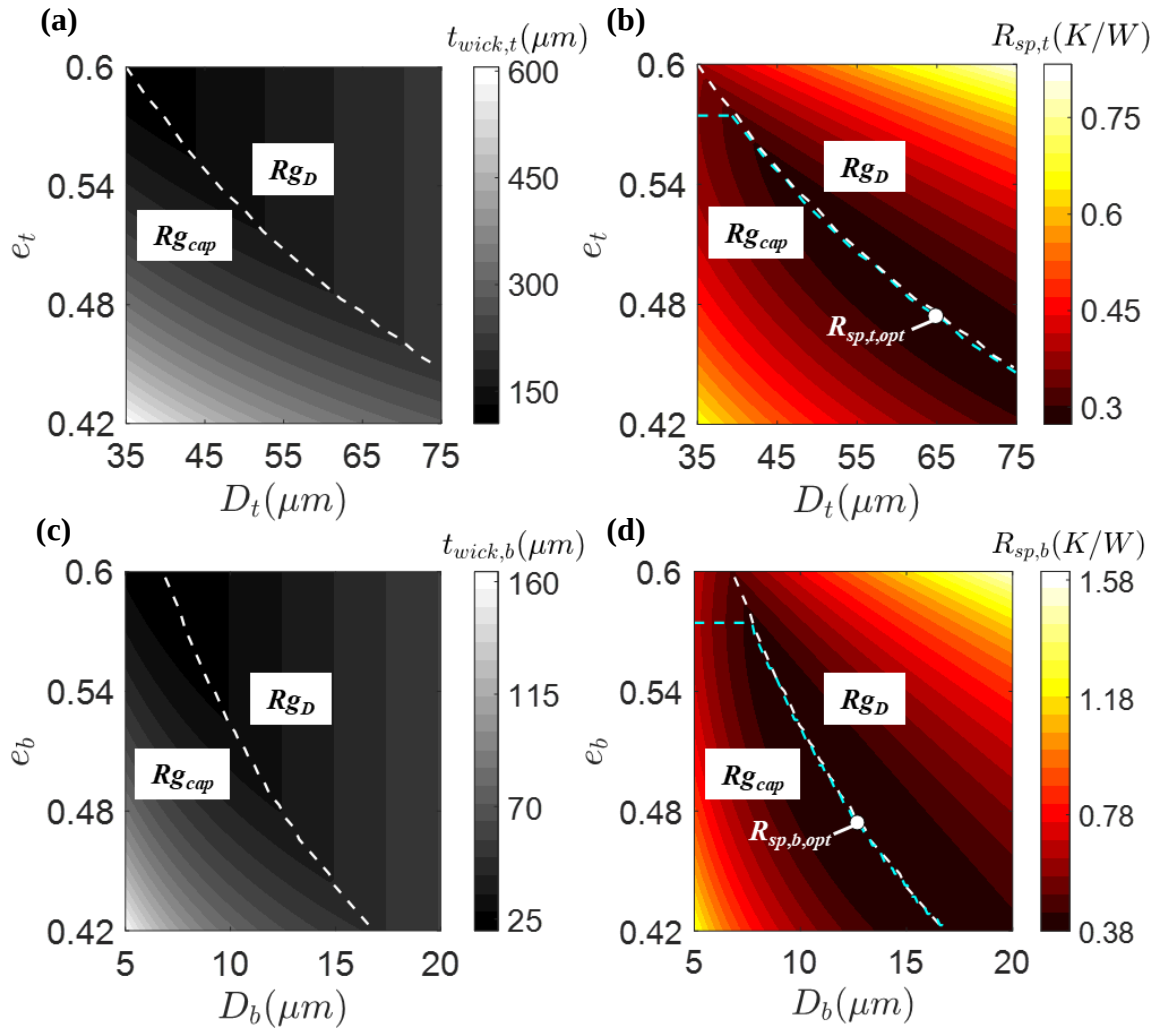

Fig. 7. (a and c) Designed wick thicknesses ($t_{wick,t}$, $t_{wick,b}$) and (b and d) maximum thermal resistances ($R_{sp,t}$, $R_{sp,b}$) for the top and bottom tiers of the cascaded multi-core vapor chamber as a function of wick porosities (e_t, e_b) and particle diameters (D_t, D_b) for total tier thicknesses t_t = 1.4 mm and t_b = 0.6 mm. The regions (Rg) to the left and right of the white dashed lines in (a) and (c) correspond to the capillary-limit-governed wick thickness (Rg_{cap}: $t_{wick,t} = t_{cap,t}$; $t_{wick,b} = t_{cap,b}$) and the particle diameter-governed wick thickness (Rg_D: $t_{wick,t} = 3D_t$; $t_{wick,b} = 3D_b$), respectively. The blue dashed lines in (b) and (d) denote the porosities (e_t, e_b) for which the thermal resistances ($R_{sp,t}$, $R_{sp,b}$) are minimum for any given particle diameters (D_t, D_b). The points of optimal thermal resistance for the top tier and the bottom tier of the cascaded multi-core vapor chamber are denoted by the white dots labeled $R_{sp,t,opt}$ and $R_{sp,b,opt}$ in (b) and (d) respectively.

The dependence of the thermal resistance (R_{sp}) of the CMVC on the core diameter ($d_{cond,b}$) is depicted in Fig. 8. Note that for each core diameter, the wick porosities (e_t, e_b) and particle diameters (D_t, D_b) are optimized to obtain the minimum thermal resistance. The results in Fig. 8 are evaluated for a fixed bottom-tier thickness of 0.6 mm. However, within a given range of bottom-tier thickness (~0.4 mm< t_b < ~1.2 mm), it was confirmed that the optimal thermal resistance (R_{sp}) of the CMVC remains nearly invariant for a given core diameter ($d_{cond,b}$). This is attributed to the dominance of the conduction resistance across the wicks relative to the vapor core thermal resistance in that range.

With an increase in the core diameter ($d_{cond,b}$), there is an increase in the optimum thermal resistance of the bottom tier ($R_{sp,b,opt}$). However, there is a simultaneous reduction in the optimum top-tier thermal resistance ($R_{sp,t,opt}$) and an increase in the heat input (Q_{chs}) at the bottom-tier core above the hotspot. Consequently, the optimal core diameter is governed by this tradeoff. Nevertheless, Fig. 8 indicates that the thermal performance of the CMVC is not overly sensitive to the core diameter for the power map investigated, having a wide range from ~3.4 mm < $d_{cond,b}$ < ~7.9 mm where the thermal resistance is within 10% of the optimum, which is attractive from a design and fabrication standpoint.

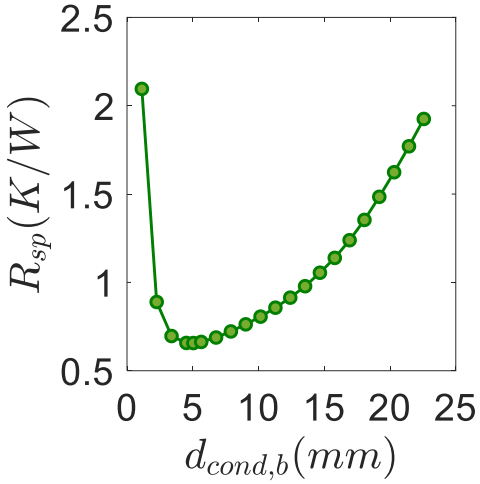

Fig. 8. Variation of the maximum thermal resistance (R_{sp}) of the CMVC with the core diameter ($d_{cond,b}$) for a bottom-tier thickness (t_b = 0.6 mm). At each core diameter, wick porosities (e_t, e_b) and the particle diameters (D_t, D_b) are optimized.

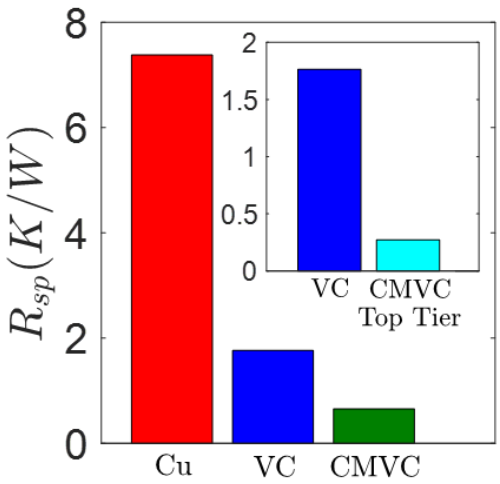

Fig. 9. Comparison of the heat spreader thermal resistance for the solid copper benchmark (Cu), conventional single-core vapor chamber (VC), and cascaded multi-core vapor chamber (CMVC). The inset shows a significant reduction in the thermal resistance of the top tier from the conventional single-core vapor chamber (VC) to the cascaded multi-core vapor chamber (CMVC).

Fig. 9 compares the predicted thermal resistance of the CMVC to the conventional single-core vapor chamber (VC) and solid copper (Cu) benchmark. The thermal resistance is largest (7.38 K/W) for the solid copper benchmark, and the optimized conventional vapor chamber offers a reduction to (1.76 K/W). This is attributed to a significant reduction in the thermal resistance of the vapor core, compared to the conduction spreading resistance in solid copper. This significant reduction in thermal spreading resistance from the solid copper to the vapor core is able to overcompensate for the penalty of the additional through-plane conduction resistance of the porous wicks of the vapor chamber. From the conventional vapor chamber to the optimized design of the CMVC, there is a further significant reduction in the total thermal resistance to 0.66 K/W. In the optimized design, the local dampening of the hotspot flux densities by the bottom-tier vapor core array results in an order of magnitude reduction of thermal resistance from 1.76 K/W for the conventional vapor chamber to only 0.27 K/W (see Fig. 9 inset) for the top tier in the CMVC. The presence of multiple cores in the bottom tier results in a high capillary limit of individual vapor cores. Consequently, this enables significantly thinner wicks having a lowered conduction resistance. Hence, the bottom tier can spread hotspots at a low thermal resistance of 0.4 K/W. Hence, there is a net overall decrease considering both the top and bottom tiers in the CMVC.

IV. Conclusion

A cascaded multi-core vapor chamber (CMVC), integrated into the lid of a heterogeneous package for the simultaneous intra-package spreading of high heat fluxes and dissipating high total powers, is optimized and evaluated relative to existing heat spreaders. The CMVC comprises a single-core vapor chamber having a relatively thick wick that is capable of managing high total heat loads and spreads them to the base of the mounted heat sink. This single-core vapor chamber is stacked on an array of smaller footprint vapor cores designed to spread multiple arbitrarily distributed high flux hotspots before they enter the top vapor chamber. Attenuation of the hotspot heat fluxes within the bottom tier array, which have relatively thin wicks, thereby avoids the large thermal resistance that would be otherwise incurred by directly subjecting the thick wick in the top tier to hotspots. Experiments conducted with commercial vapor chambers confirm the enhancement in the performance of a given vapor chamber through successive stacking of vapor chambers with increasing footprints, thereby motivating the CMVC concept. An experimentally validated reduced-order model is used to estimate the performance of the CMVC, as well as to survey the design space to minimize its thermal resistance. The wick properties and geometric parameters of the CMVC are varied to optimize the thermal performance of the CMVC for the representative power map. The optimized intra-lid cascaded multi-core vapor chamber is predicted to provide a significant reduction in thermal resistance compared to solid copper heat spreaders and conventional single-core vapor chambers. This optimization process revealed the higher sensitivity of the optimized thermal resistance with respect to wick porosity compared to the particle diameter. Importantly, the parametric optimization of the CMVC design for the single power map in the present study reveals the existence of the wide range of wick properties and vapor core dimensions that provided near-optimal performance. This indicates the adaptability of the concept of using a cascade of vapor chambers for differing power maps comprising multiple characteristic heat flux levels.

ACKNOWLEDGMENT

This material is based upon work supported by Semiconductor Research Corporation (SRC), as a part of the Global Research Collaboration (GRC) Program on Packaging (PKG; Science Director, Dr. John Oakley) in the Center for Heterogeneous Integration Research on Packaging (CHIRP). We are thankful to our SRC liaisons for their discussion and input on the work.

REFERENCES

[1] Bar-Cohen, A., 2013, Gen-3 Thermal management technology: role of microchannels and nanostructures in an embedded cooling paradigm. *Journal of Nanotechnology in Engineering and Medicine*, 4(2), p. 20907.

[2] Weibel, J.A. and Garimella, S.V., 2013. Recent advances in vapor chamber transport characterization for high-heat-flux applications. *Advances in Heat Transfer*, 45, pp. 209-301.

[3] Faghri, A., 1995. *Heat Pipe Science and Technology*. Taylor & Francis, Washington, DC.

[4] Weibel, J.A., Garimella, S.V. and North, M.T., 2010. Characterization of evaporation and boiling from sintered powder wicks fed by capillary action. *International Journal of Heat and Mass Transfer*, 53(19-20), pp.4204-4215.

[5] Li, C., Peterson, G. P., and Wang, Y., 2006, Evaporation/Boiling in thin capillary wicks (l) – wick thickness effects, *Journal of Heat Transfer*, 128(12), pp. 1312–1319.

[6] Li, C., Peterson, G. P., and Wang, Y., 2006, Evaporation/Boiling in thin capillary wicks (II) – wick thickness effects, *Journal of Heat Transfer*, 128(12), pp. 1312–1319.

[7] Chen, Y.T., Kang, S.W., Hung, Y.H., Huang, C.H. and Chien, K.C., 2013. Feasibility study of an aluminum vapor chamber with radial grooved and sintered powders wick structures. *Applied Thermal Engineering*, 51(1-2), pp.864-870.

[8] Hwang, G.S., Nam, Y., Fleming, E., Dussinger, P., Ju, Y.S., and Kaviany, M., 2010. Multi-artery heat pipe spreader: experiment. *International Journal of Heat and Mass Transfer*, 53(13-14), pp.2662-2669.

[9] Ju, Y.S., Kaviany, M., Nam, Y., Sharratt, S., Hwang, G.S., Catton, I., Fleming, E., and Dussinger, P., 2013. Planar vapor chamber with hybrid evaporator wicks for the thermal management of high-heat-flux and high-power optoelectronic devices. *International Journal of Heat and Mass Transfer*, 60, pp.163-169.

[10] Weibel, J.A. and Garimella, S.V., 2012. Visualization of vapor formation regimes during capillary-fed boiling in sintered-powder heat pipe wicks. *International Journal of Heat and Mass Transfer*, 55(13-14), pp.3498-3510.

[11] Semenic, T. and Catton, I., 2009. Experimental study of biporous wicks for high heat flux applications. *International Journal of Heat and Mass Transfer*, 52(21-22), pp.5113-5121.

[12] Sudhakar, S., Weibel, J.A., Zhou, F., Dede, E.M., and Garimella, S.V., 2019. Area-scalable high-heat-flux dissipation at low thermal resistance using a capillary-fed two-layer evaporator wick. *International Journal of Heat and Mass Transfer*, 135, pp.1346-1356

[13] Sudhakar, S., Weibel, J.A., Zhou, F., Dede, E.M., and Garimella, S.V., 2020. The role of vapor venting and liquid feeding on the dryout limit of two-layer evaporator wicks. *International Journal of Heat and Mass Transfer*, 148, p.119063.

[14] Cai, Q. and Bhunia, A., 2012. High heat flux phase change on porous carbon nanotube structures. *International Journal of Heat and Mass Transfer*, 55(21-22), pp.5544-5551.

[15] Cai, Q. and Chen, Y.C., 2012. Investigations of biporous wick structure dryout. *Journal of Heat Transfer*, 134(2), p.021503.

[16] Palko, J.W., Zhang, C., Wilbur, J.D., Dusseault, T.J., Asheghi, M., Goodson, K.E., and Santiago, J.G., 2015. Approaching the limits of two-phase boiling heat transfer: high heat flux and low superheat. *Applied Physics Letters*, 107(25), p.253903.

[17] Bandyopadhyay, S., Marconnet, A.M., and Weibel, J.A., 2020, July. A cascaded multi-core vapor chamber for intra-lid heat spreading in heterogeneous packages. *19th IEEE Intersociety Conference on Thermal and Thermomechanical Phenomena in Electronic Systems (ITherm) IEEE.*

[18] Lee, S., 1995. Optimum design and selection of heat sinks. *IEEE Transactions on Components, Packaging, and Manufacturing Technology*: Part A, 18(4), pp.812-817.

[19] Song, S., Au, V., and Moran, K.P., 1995. Constriction/spreading resistance model for electronics packaging. *Proceedings of the 4th ASME/JSME Thermal Engineering Joint Conference*, pp. 199-206.

[20] Patankar, G., Weibel, J.A., and Garimella, S.V., 2017. Working- fluid selection for minimized thermal resistance in ultra-thin vapor chambers. *International Journal of Heat and Mass Transfer*, 106, pp.648-654.

[21] Sarangi, S., Weibel, J.A., and Garimella, S.V., 2015. Effect of particle size on surface-coating enhancement of pool boiling heat transfer. *International Journal of Heat and Mass Transfer*, 81, pp.103-113.

Soumya Bandyopadhyay received the Integrated B.Tech. and M.Tech. degrees in mechanical engineering from IIT Kharagpur, India, in 2018. He is currently a graduate student working with Dr. Justin A. Weibel at the Cooling Technologies Research Center, School of Mechanical Engineering, Purdue University, West Lafayette, IN, USA. As a part of graduate work, he is working on designing thermal solutions for heterogeneous system-in-package architectures in modern electronic devices. His general interests are in the system- and component-level mechanical design of products for commercial applications.

Amy M. Marconnet is an Associate Professor in the in the School of Mechanical Engineering at Purdue University. She received the B.S. degree in mechanical engineering from the University of Wisconsin—Madison in 2007, and the M.S. and Ph.D. degrees in mechanical engineering from Stanford University in 2009 and 2012, respectively. She was a Post-Doctoral Associate with the NanoEngineering Group, Massachusetts Institute of Technology, from 2012 to 2013, before joining the faculty of the School of Mechanical Engineering at Purdue University. Her current research interests include thermal transport and energy conversion in multi-scale and heterogeneous systems. She was recognized as the 2017 Woman Engineer of the Year from the ASME Electronics & Photonics Packaging Division, the 2020 Outstanding Faculty Mentor of Engineering Graduate Students from the College of Engineering at Purdue, and the 2020 Bergles-Rohsenow Young Investigator Award in Heat Transfer from ASME.

Justin A. Weibel is a Research Associate Professor in the School of Mechanical Engineering at Purdue University and Director of the Cooling Technologies Research Center (CTRC), a graduated NSF I/UCRC. He received his PhD in 2012 and BSME in 2007, both from Purdue University. Dr. Weibel's research explores methodologies for prediction and control of heat transport to enhance the performance and efficiency of thermal management technologies and energy transfer processes. Dr. Weibel has supervised over 30 PhD and MS students and co-authored over 140 referred journal and conference papers. He was recently recognized as an Outstanding Engineering Teacher by the College of Engineering at Purdue University and received the 2020 ASME Electronic & Photonic Packaging Division (EPPD) Young Engineer Award. He is an Associate Editor of the IEEE Transactions on Components Packaging and Manufacturing Technology.